

EXPLORING THE KINEMATICS OF THE OXYGEN-RICH SUPERNOVA REMNANT G292.0+1.8: EJECTA SHELLS, FAST-MOVING KNOTS AND SHOCKED CIRCUMSTELLAR MATERIAL

PARVIZ GHAVAMIAN¹, JOHN P. HUGHES^{2,3} AND T. B. WILLIAMS^{2,3}

Revised Version, August 13, 2005

ABSTRACT

We present results of an in-depth optical study of the core collapse supernova remnant G292.0+1.8 using the Rutgers Fabry-Perot (RFP) imaging spectrometer. Our observations provide a detailed picture of the supernova remnant in the emission lines of [O III] $\lambda 5007$, H α and [N II] $\lambda 6548$. The [O III] Fabry-Perot scans reveal a bright crescent-shaped spur of previously known high-velocity ($V_{\text{radial}} \sim 1500 \text{ km s}^{-1}$) O-rich ejecta located on the eastern side of the remnant. The spur consists of a semi-coherent structure of mostly redshifted material, along with several clumps that have apparently broken out of the more orderly shell-like expansion. The high velocity ($\gtrsim 600 \text{ km s}^{-1}$) component of the spur also displays a scalloped morphology characteristic of Rayleigh-Taylor instabilities. We also find a large number of fast-moving knots (FMKs) of O-rich ejecta undetected in prior photographic plate images and similar to features seen in Cas A. The FMKs are distributed sparsely in the interior of G292.0+1.8 and are seen mostly in blueshifted emission out to $V_{\text{radial}} \approx -1700 \text{ km s}^{-1}$. The position-velocity distribution of the FMKs can be kinematically described as a shell $3/4$ in radius expanding at a velocity of 1700 km s^{-1} . Another feature apparent in the [O III] scans is an equatorial belt consisting of both a bar-like structure at zero radial velocity and a clumpy, high velocity ejecta component seen in projection along the line of sight. Portions of the zero-velocity bar are spatially well correlated with a similar structure seen in the *Chandra* X-ray image of G292.0+1.8. The bar is also detected in our H α RFP images at zero radial velocity, providing further evidence that this structure is of circumstellar origin. We find that the optical and X-ray properties of the bar are consistent with incomplete (partially radiative) shocks in material of moderate densities. There are also a number of faint, elongated structures seen in H α at zero radial velocity across the interior of G292.0+1.8 that lack [O III] and X-ray counterparts. These filaments may be low-density H I clouds photoionized by hard radiation from the interior of the remnant. Overall these results suggest that G292.0+1.8 is currently interacting with a low density environment. We find no evidence for high velocity H α or [N II] emission over the dynamical range sampled by the RFP. Assuming a distance of 6 kpc for G292.0+1.8, we estimate a kinematic age of $(3000\text{--}3400) d_6$ years for this remnant.

Subject headings: supernova remnants — ISM: individual (G292.0+1.8)

1. INTRODUCTION

Among the known supernova remnants (SNRs), a handful contain fast-moving debris with optical spectra dominated by lines of oxygen and its associated burning products. In these metal-rich remnants, the emission is produced by excitation of dense material from deep within the massive progenitor star ($\gtrsim 10 M_{\odot}$), laid bare by the supernova explosion. Dense clumps of ejecta coast along mostly intact and undecelerated until they penetrate the hot, overpressured gas of the reverse shock. As shocks are driven into the fragments they are torn apart into clumps of varying size and density. The densest material ($n \gtrsim 10 \text{ cm}^{-3}$, $V_{\text{shock}} \sim 100 \text{ km s}^{-1}$) produces optical/UV spectra dominated by very strong oxygen line emission, with little or no emission from lines of H, He and N commonly seen in shocked interstellar material. The spectroscopic study of ejecta material in oxygen-rich supernova remnants (OSNRs) provides us with a rare opportunity to study both

the kinematics of the supernova ejecta and the products of both hydrostatic and explosive nucleosynthesis in massive stars.

To date there have been six OSNRs identified: Cassiopeia A (Minkowski 1957, Chevalier & Kirshner 1978, 1979, Reed et al. 1995, Fesen et al. 2001), Puppis A (Winkler & Kirshner 1985) and G292.0+1.8 (Goss et al. 1979, Murdin & Clark 1979, van den Bergh 1979, Braun et al. 1983, Dopita & Sutherland 1995) in the Galaxy, 0540–69.3 (Kirshner et al. 1989) and N132D (Lasker 1978, 1980; Morse, Winkler & Kirshner 1995; Morse et al. 1996; Blair et al. 2000) in the LMC, E0102–72.2 in the SMC (Dopita, Tuohy & Mathewson 1981, Tuohy & Dopita 1983, Blair et al. 2000) and a spatially unresolved remnant in NGC 4449 (Kirshner & Blair 1980, Blair Kirshner & Winkler 1983). Although the core-collapse supernovae which produced these OSNRs should have all left behind rotating neutron stars (pulsars), G292.0+1.8 is the only

¹Department of Physics and Astronomy, Johns Hopkins University, 3400 North Charles Street, Baltimore, MD, 21218-2686; parviz@pha.jhu.edu

²Department of Physics and Astronomy, Rutgers University, Piscataway, NJ 08854-8019; jph@physics.rutgers.edu, williams@physics.rutgers.edu

³Visiting Astronomer, Cerro Tololo Inter-American Observatory, National Optical Astronomy Observatories. CTIO is operated by AURA, Inc. under contract to the National Science Foundation.

Galactic remnant from this class found to harbor both an active pulsar (Camilo et al. 2002, Hughes et al. 2003) and associated pulsar wind nebula (PWN) (Hughes et al. 2001). Earlier *Einstein* HRI observations indicated that a central bar of enhanced X-ray emission was present in G292.0+1.8, superimposed on an ellipsoidal disk of emission (Tuohy, Clark & Burton 1982). Recent *Chandra* imagery of G292.0+1.8 (Park et al. 2002, 2004; Gonzalez & Safi-Harb 2003) have revealed that the X-ray bar is of normal composition, suggesting that G292.0+1.8 is interacting with circumstellar wind material. On the basis of the rich variety of physical processes present in G292.0+1.8 (O-rich optical and X-ray emission, active pulsar/PWN and apparent circumstellar interaction) one may argue that G292.0+1.8 is the best SNR for a simultaneous study of all aspects of core collapse supernova explosions.

As with many supernova remnants known today, G292.0+1.8 was first discovered in a radio survey (Mills, Slee & Hill 1961). The first followup radio observations (Lockhart et al. 1977) showed a center-filled (plerionic) morphology, leading some to conclude that the remnant was “Crab-like”, i.e., that synchrotron radiation from a PWN dominated the radio appearance of the SNR. However, further radio observations by Braun et al. (1986) demonstrated that there are two components to the radio morphology of G292.0+1.8: a bright circular region near the center approximately $4'$ across embedded in a surrounding fainter plateau of emission approximately $8'$ across. In a more recent *Chandra* observation of G292.0+1.8, Hughes et al. (2001) discovered a point source of hard X-ray emission near the geometric center surrounded by a nonthermal halo $1' - 2'$ across. They argued that the source was a pulsar and PWN, a conclusion which was confirmed by discovery of 135 ms radio pulsations from the point source, now designated PSR J1124–5916 (Camilo et al. 2002; Hughes et al. 2003). Subsequently Gaensler & Wallace (2003; hereafter GW03) showed that the spectral index of the bright radio core is consistent with synchrotron radiation from a PWN ($\alpha = -0.05$), while the index of the plateau is steep ($\alpha = -0.5$), consistent with particle acceleration in shocks.

X-ray emission from the metal-rich ejecta in G292.0+1.8 was first detected in *Einstein* data (Clark, Tuohy, & Becker 1980). Detailed X-ray spectroscopy was performed by Hughes & Singh (1994), who showed that the global X-ray spectrum of G292.0+1.8 was dominated by K-shell line emission from metal-rich ejecta. Based on abundances derived from their global spectral models, Hughes & Singh (1994) argued that the ejecta composition of G292.0+1.8 matched the yields of $20 M_{\odot}$ nucleosynthesis models best. However, in a recent analysis of *Chandra* spectra of G292.0+1.8 Park et al. (2004), noting that only the X-ray lines of O, Ne, Mg and Si were detected, suggested that the reverse shock has not yet penetrated beyond the layers of hydrostatically burned material. Since knowledge of the relative abundances of both hydrostatic and explosive burning products are required for an accurate estimate of the progenitor mass from the supernova nucleosynthesis models, Park et al. (2004) concluded that the progenitor mass estimate by Hughes & Singh (1994) was no longer reliable. Thus the mass of the progenitor star of G292.0+1.8 remains uncertain.

The first optical imagery of G292.0+1.8 was performed

by Goss et al. (1979), who discovered a bright, crescent-shaped spur of nebulosity coincident with the extended radio source position. Their spectra showed emission lines of oxygen and neon, but little or no line emission from hydrogen, helium or nitrogen. Followup spectra of the spur acquired by Murdin & Clark (1979), van den Bergh (1979), Braun et al. (1983) and Sutherland & Dopita (1995) showed broad [O III] lines extending over a velocity range $\sim 2000 \text{ km s}^{-1}$. Narrowband optical CCD images of G292.0+1.8 have recently been acquired by Winkler & Long (2005; hereafter WL05). According to all these studies, the optical appearance of G292.0+1.8 is dominated by radiative shocks in dense supernova ejecta which have undergone negligible mixing with the ISM.

In this paper, we report results of Rutgers Fabry-Perot (RFP) imaging spectroscopy of G292.0+1.8 in emission lines of [O III], $H\alpha$, and [N II]. Both the narrowband [O III] imagery of WL05 and our RFP scans have revealed extensive oxygen-rich material undetected in the earlier photographs, including previously undetected knots of O-rich ejecta similar to those seen in Cas A and an equatorial belt of shocked material. As we will show, the compact knots of O-rich ejecta exhibit large radial velocities ($\sim 1500 \text{ km s}^{-1}$), showing that these features are fast-moving knots (FMKs). In addition, we will show that the zero velocity [O III] and $H\alpha$ emission from the equatorial belt trace a bar-like structure matching a similar feature in the X-ray band. This confirms the assertions of Park et al. (2002, 2004) and Gonzalez & Safi-Harb (2003) that this feature is comprised of circumstellar material. The velocity range of both the FMKs and the bright O-rich spur extends over a 50% broader range in velocities than previously determined for G292.0+1.8 (Murdin & Clark 1979, van den Bergh 1979), extending to $\sim 3000 \text{ km s}^{-1}$. Throughout this paper we assume a distance of 6 kpc to G292.0+1.8 (GW03) and quote distance-dependent quantities in units of 6 kpc.

2. OBSERVATIONS AND DATA REDUCTION

Our observations of G292.0+1.8 were performed with the RFP spectrometer at the 1.5 m telescope of Cerro Tololo Inter-American Observatory. The $H\alpha$ data were acquired on the night of 1998 February 17 (UT), while the [O III] data were acquired on the nights of 1998 February 20 and 21 (UT). The Tek1024 CCD and 200 mm camera lens were used with the f/7.5 secondary focus, giving an image scale of $0''.65 \text{ pixel}^{-1}$ for all the observations. The field of view was a circle $7/8$ in diameter, centered on coordinates $11^{\text{h}}24^{\text{m}}30^{\text{s}}.5$, $-59^{\circ}16'01''.3$ (2000) for the $H\alpha$ scans and $11^{\text{h}}24^{\text{m}}24^{\text{s}}.2$, $-59^{\circ}16'08''.8$ (2000) for the [O III] scans. In Figure 1 the RFP field of view is marked on the continuum-subtracted narrowband [O III] image of WL05. The broad etalon was used during all RFP observations. The $H\alpha$ scans sampled the emission at 19 velocities from -800 km s^{-1} to $+570 \text{ km s}^{-1}$, at intervals of 70 km s^{-1} per sample. The [O III] scans were centered on 5007 \AA and ranged from -1435 km s^{-1} to $+1675 \text{ km s}^{-1}$, sampling the emission from G292.0+1.8 in 29 samples over 100 km s^{-1} intervals. During our observations we isolated emission from a single spectral order using CTIO [O III] filter 4993/44 ($\Delta \lambda_c = 44 \text{ \AA}$) for scans centered in the range $4983 \text{ \AA} \leq \lambda \leq 5001 \text{ \AA}$, filter 5007/44 for scans in the range

$5003 \text{ \AA} \leq \lambda \leq 5019 \text{ \AA}$ and $5037/44$ for scans in the range $5021 \text{ \AA} \leq \lambda \leq 5035 \text{ \AA}$. On the first night of the [O III] observations the median seeing was $1''.9$, during which we acquired the scans between -250 km s^{-1} and $+710 \text{ km s}^{-1}$. The remaining FP scans were obtained during the second night of [O III] observations, when the seeing had worsened to $2''.6$. Two 500 s frames were acquired at each RFP etalon setting in both [O III] and $\text{H}\alpha$ /[N II].

We reduced the Fabry-Perot images using IRAF⁴ and our own custom software. Each pair of FP scans was combined in IRAF using the `creject` option to remove cosmic rays and create images with an effective exposure time of 1000 s. We applied overscan and bias subtraction to all images in the standard way. Separate flat field images of the telescope dome white spot were obtained at each observed wavelength, and were used to correct the detector pixel-to-pixel response variations and to remove the filter transmission function. The wavelength scale was calibrated using a series of comparison lamp exposures of nearby $\text{H}\alpha$ and neon emission lines. The zero-point drift of the wavelength solution was determined from $\text{H}\alpha$ and Neon calibration exposures interspersed with the object frames during the observations. We estimate that the resulting wavelength calibration is accurate to better than 0.1 \AA . The RFP instrumental spectral profile measured from the calibration exposures is well fit by a Voigt function with a Gaussian width of 44 km s^{-1} and Lorentzian width of 52 km s^{-1} . The resulting instrumental FWHM is 117 km s^{-1} . We scaled the transmission of the RFP scans to a common airmass using the CTIO mean extinction tables. The variations in transparency between frames was tracked via photometry of unsaturated stars in the field. From the photometry we calculated the multiplicative constants required to bring the fluxes from all frames to a common level. Next, we applied a Gaussian smoothing kernel to each combined scan to produce a common effective seeing of $3''.0$ FWHM. Finally we computed a coordinate solution (accurate to within $0''.2$) for each image using seven USNO–A2.0 Catalogue stars distributed over the field of view.

Several factors complicate the identification of [O III] emission features in our RFP scans. G292.0+1.8 lies in a rich stellar field and the sizes of many emission knots are comparable to the seeing FWHM, so there is a significant danger of mistaking stars for emission knots (and vice versa). In addition, internal reflections within the etalon cause ghosts (mirror images) of the brightest stars to be projected across the optical axis in each frame, further complicating the identification of [O III] knots. To minimize these problems, we first subtracted the stars from each [O III] RFP scan using a background image created by median combining three FP scans devoid of any obvious line emission from the SNR and the night sky. Scaling the background image by a multiplicative constant and subtracting it from each of the 28 [O III] RFP scans, we generated a set of continuum-subtracted images. This process removes approximately 90% of the stars from each frame, leaving only residuals from the brightest stars and their ghosts. The ghosts were identified by tracing the reflection of each bright star across the FP axis, then re-

moved by interpolating the surrounding sky emission over the ghost feature. We were able to check the completeness of our ghost removal by registering and comparing our individual FP scans with blue DSS images.

3. CONSTANT VELOCITY SNAPSHOTS OF G292.0+1.8

Much of the ejecta material in G292.0+1.8 exhibits a morphology that varies strongly with velocity and position. To map this distribution we found it useful to extract snapshots of the entire remnant at a selected range of velocities. The wavelength of the FP transmission profile is not constant over the field but shortens quadratically from the optical axis to the edge of each frame, amounting to a 200 km s^{-1} blueshift in our [O III] observations. Thus, to create the single velocity images we interpolated the flux at each point in the field using RFP scans bracketing the desired velocity. To minimize source confusion we used the continuum-subtracted RFP scans to generate the constant velocity [O III] images. Due to variations in sky emission between adjacent scans, the interpolation introduces a slight ringing effect into some constant velocity images, i.e., some images show annular strips where the average pixel value differs from the value in the adjacent region. We applied a first order correction to the background by adding a constant pixel value to the mismatched annular regions. This brought the background pixel values in all the interpolated strips to within roughly 20% of one another. Although this procedure did not correct for interpolation errors in the object emission and left some residual structure in the background, it was sufficient to allow easy identification of supernova remnant emission at each velocity interval. We were able to verify that for a given constant velocity image the brightest emission knots do correctly appear at the velocity centroids measured from line profile fits to the knots (described in Section 5). To remove any further stellar residuals which may be mistaken for FMKs, we interpolated the background over the positions of the brightest subtracted stars in the RFP field of view. We examined the remaining knots visible in the image sequence of Figure 2 and verified that the flux from each knot followed the sequential rise and fall expected of real emission lines in the RFP frames.

4. GLOBAL DISTRIBUTION OF THE O-RICH EJECTA

To illustrate the dependence of the global ejecta distribution on radial velocity, we present a sequence of constant velocity [O III] images in Figure 2. The sequence is arranged in order of heliocentric radial velocity, from blue to red, in increments of 120 km s^{-1} (roughly the instrumental profile FWHM). The sequence extends to $\pm 1440 \text{ km s}^{-1}$, although there is a highly blueshifted knot near the center of G292.0+1.8 still visible blueward of -1440 km s^{-1} and a similar, but much fainter knot, detected at $+1700 \text{ km s}^{-1}$ (marked K1 and K2, respectively, in Figure 1). The faint, diffuse [O III] emission first detected by Murdin & Clark (1979) is clearly visible in the image at zero radial velocity (corresponding to zero heliocentric velocity, or $V_{LSR} = 4.5 \text{ km s}^{-1}$). The diffuse [O III] does not appear at other velocities and extends beyond the edge of the SNR shell defined by the X-ray and radio observations.

⁴IRAF is distributed by the National Optical Astronomy Observatories, which is operated by the AURA, Inc. under cooperative agreement with the National Science Foundation

This suggests that the diffuse emission is produced by photoionized interstellar gas, in agreement with the conclusion of Murdin & Clark (1979).

Based on the single velocity images in Figure 2, the shocked [O III] emission in G292.0+1.8 can be broadly placed into three categories:

(1) A bright, curved structure located on the eastern edge of G292.0+1.8 and exhibiting a broad velocity dispersion ($\gtrsim 2000 \text{ km s}^{-1}$; Murdin & Clark 1979). Spectroscopic observations of this spur showed only emission lines of O and Ne (Murdin & Clark 1979, van den Bergh 1979, Braun et al. 1983, Sutherland & Dopita 1995), indicating that the material was stellar ejecta uncontaminated by interstellar material. The earliest published spectra showed that the spur consists of predominantly redshifted material. The RFP scans presented in this paper confirm this result and show that the spur traces a semi-coherent structure at redshifted velocities, moving progressively inward (toward the center of G292.0+1.8) with increasing radial velocity. This trend is consistent with the geometric projection expected from an expanding shell. A new feature, unseen in the earlier photographic images of G292.0+1.8 (Goss et al. 1979; Tuohy, Clark & Burton 1982) but clearly detected both in the [O III] image (Figure 1) and our RFP scans (Figure 2), is the collection of ‘streamers’ seen radiating southward from the innermost edge of the spur. The streamer emission also moves inward with progressively larger redshift, suggesting that these features trace a partially complete shell similar to the spur.

(2) An equatorial belt running E-W along the projected center of the X-ray remnant. The optical belt appears as a clumpy line of broken filaments in Figure 1. It is kinematically resolved into multiple components by our RFP observations in Figure 2: a bar-shaped structure of material at zero radial velocity, projected onto a high velocity component of clumpy material. Due to its intrinsic faintness, the belt emission escaped detection in the earlier photographic plate images of G292.0+1.8 (Goss & Shaver 1979; Tuohy, Clark & Burton 1982). As we will show, the bar seen in our RFP scans appears to be the optical counterpart to the bar seen in the *Chandra* images by Park et al. (2002, 2004) and Gonzalez and Safi-Harb (2003). The appearance of both the bar and the diffuse emission over most of the field at zero radial velocity suggests that the bar also lies in the G292.0+1.8 rest frame. This is consistent with a slow wind ($V \lesssim 10 \text{ km s}^{-1}$) origin for the bar.

(3) Fast-moving knots (FMKs, in analogy to similar features in Cas A; Chevalier & Kirshner 1978) seen in [O III] (but not H α) out to radial velocities $\sim \pm 1500 \text{ km s}^{-1}$. These conspicuous features are clearly seen in the narrowband [O III] image (Figure 1), above and below the equatorial belt. In the RFP data the FMKs range in size from around $5''$ down to the seeing limit of $3''$. A clear trend in the FMK velocity distribution of Figure 2 is that nearly all of the northern FMKs are either seen at zero velocity or are blueshifted, while most (but not all) of the southern FMKs are either seen at zero velocity or are redshifted. Unlike what is observed in Cas A (Reed et al. 1995; Lawrence et al. 1995; Fesen et al. 2001), the FMKs in G292.0+1.8 are more isolated and sparsely distributed across the remnant. Aside from the spur, there are no networks of curved ejecta filaments associated with the FMKs

as seen in Cas A (Fesen et al. 2001).

Although the velocity image sequence is a useful tool for exploring the ejecta emission on a global scale, exploring the kinematics of individual knots and the dynamical processes affecting them (e.g., shear, dynamical instabilities, etc.) is easiest when a sequence of ejecta knot images are arranged side by side in velocity as 2-dimensional spectra. We used the continuum-subtracted RFP scans to construct an image sequence of selected features including FMKs, sections of the spur and portions of the equatorial belt. In Figure 3 we present a set of ten spectra consisting of images $11'' \times 11''$ in size. The sequence includes the most blueshifted and redshifted knots detected in the RFP images (K1 and K2, corresponding to spectra 1 and 10, respectively). There is clear evidence of velocity shear seen in spectrum 6 from the spur: emission extending redward from -100 km s^{-1} to $+600 \text{ km s}^{-1}$. In the remaining spectra the faint, photoionized gas surrounding G292.0+1.8 is clearly visible near zero radial velocity (particularly in spectra 1 and 9). In spectrum 3 a pattern can be seen in the FMK emission where the top of the clump first appears at around -1200 km s^{-1} , then the lower portions progressively appear at increasingly redshifted velocities. Spectrum 10 illustrates the spatial superposition between the zero velocity bar emission and the high velocity ejecta (knot K1) present in the equatorial belt.

5. SPECTRA AND [O III] LINE PROFILE FITS

To perform a detailed kinematic analysis of G292.0+1.8 we extracted spectra from both the spur and the individual FMKs and fit the [O III] line profiles. Although the star subtraction process used to create the single velocity images in Figure 2 was adequate for the task of revealing the ejecta distribution, we utilized the unsubtracted frames for the spectral extraction to better calculate the local background around each emission knot. We selected FMKs for spectral extraction by eye, taking care to avoid stellar contamination by checking that knots in the RFP scans did not appear as stars in the DSS blue image of the G292.0+1.8 field. The apertures used for the spectral extractions were $3''.2 \times 3''.2$ squares, roughly equal to the seeing FWHM of the smoothed data. The extraction apertures for the bright southeastern spur were of the same size, laid out on a grid covering the entire structure. The extraction apertures also covered the brightest knots of streamer material seen just south of the spur in Figure 1.

The spectral extraction consisted of first summing the emission within each defined extraction aperture, for each frame of the datacube. To subtract the sky emission, we selected a ring of pixels in each frame, centered on the optical axis and passing through the middle of each extraction aperture. This ensured that the sky fluxes were extracted at the same wavelength as the emission within each aperture. The ring consisted of all the sky lying off the supernova remnant which included the widespread diffuse emission but excluded stars or other detectable discrete sources. We summed the sky emission along the ring, rejecting pixels deviating more than 4σ from the mean value. We then multiplied the resulting sky spectrum by $N_{pix}(obj)/N_{pix}(sky)$ to obtain a scaled sky spectrum for each of the apertures. Subtracting this spectrum from that of each emission knot yielded the final spectrum for each aperture. The sky subtraction removes large scale

sources of background emission in the RFP data bandpass, namely Galactic [O III] and diffuse [O III] surrounding G292.0+1.8.

Routines were written to extract the [O III] profiles and subtract background emission from all the spectra. Compared to typical long-slit spectral observations (e.g., the Cas A study by Reed et al. 1995), the spectral range of our data is much shorter, covering only $\sim 52\text{\AA}$ at [OIII] and $\sim 30\text{\AA}$ at H α . In addition, our spectra are typically less than critically sampled. We fit our data with a spectral profile that included both the instrumental and expected intrinsic source profile shapes, as described below. Due to the large number of spectra obtained from both the FMKs and the spur region, it was necessary to automate the line identification and fitting process.

Most of the FMK spectra exhibited solitary [O III] emission components. However, due to the combined factors of geometrical projection and the possible action of dynamical processes within the shocked ejecta of the spur (instabilities, shear motions, etc.), the RFP spectra of the spur often exhibited [O III] emission from multiple velocity components. We did not know *a priori* the number of [O III] lines to expect in any single RFP spectrum, and therefore needed a method of determining the number of distinct significant emission lines in each spectrum. Initial trial and error showed that maxima less than 4σ above the background failed to yield stable line profile fits, so only features with higher S/N were counted as separate components. Although this eliminates the possibility of measuring radial velocities for some of the fainter emission, we were more concerned here with making reliable line identifications and measuring accurate radial velocities for well-defined features. After rejecting spectra of some of the fainter features in the RFP data, our final sample consisted of 62 FMK and 462 spur/streamer spectra. We assumed the [O III] profiles to be intrinsically Gaussian in shape; convolved with the instrumental response of the RFP the resulting profile is a Voigt function. Therefore, we fit emission lines with Voigt functions of fixed Lorentzian width (the instrumental value, 52 km s^{-1}) and left the line flux, Gaussian width, line centroid and background level as free parameters. During each profile fit we initially set the width of the Gaussian component equal to the instrumental value and the line centroid equal to the velocity of the local flux peak.

The Gaussian widths yielded by our fits to all the [O III] profiles ranged from close to the instrumental Gaussian width (44 km s^{-1}) to values around 100 km s^{-1} , with a few profiles exhibiting widths as large as 350 km s^{-1} . Overall, the line widths are consistent with [O III] emission from radiative shocks with $V_S \sim 50\text{--}200\text{ km s}^{-1}$, although the large widths of some of the emission lines may be produced by blending of narrower features. In Figures 4 and 5 we present examples of spectra from nine FMKs and sixteen locations in the spur, along with the line profile fits obtained using the method described above.

Although the main goal of the RFP observations was to map the [O III] $\lambda 5007$ emission in G292.0+1.8, it is not known whether other emission lines could have been shifted into the bandpass of our spectra. Optical studies of other OSNRs such as Cas A (Reed et al. 1995) have shown that the emission lines from some ejecta knots may

be Doppler shifted enough to cause ambiguity in distinguishing lines of one atomic species from those of another. Obviously this is also a potential concern for G292.0+1.8, where some features in our RFP spectra may be classified as either highly blueshifted [O III] $\lambda 5007$ emission or highly redshifted [O III] $\lambda 4959$ emission. In this study we assume that all the bright spectral lines we have fitted are due to the [O III] $\lambda 5007$ transition. It is possible that this has produced an error in the computed radial velocity (by $+2900\text{ km s}^{-1}$ if we have misidentified as $\lambda 5007$ what is actually a $\lambda 4959$ transition). Resolving this potential ambiguity would require additional spectroscopy over a wider spectral band. For the ensemble of knots, however, we believe that this is unlikely to be an important or widespread effect. As we show in the next section, the identification of the FMK spectral features as $\lambda 5007$ lines leads to a simple kinematic picture of the FMKs, and yields an age for G292.0+1.8 consistent with the age predicted by recent global models of the supernova remnant/PWN energetics (Chevalier 2005).

6. RADIAL VELOCITIES OF THE EJECTA DISTRIBUTION

6.1. FAST-MOVING KNOTS

Using the [O III] line profile fits, we calculated the radial velocities of the 62 selected FMKs and plotted the velocities as a function of the knots' radial distance from the geometric center $(\alpha, \delta) = 11^{\text{h}}24^{\text{m}}34^{\text{s}}.68, -59^{\circ}15'29''$ (2000) for G292.0+1.8 as determined from the radio observations of GW03. We present a position-velocity diagram of the FMKs in Figure 6. The correlation observed between FMK velocities and their distances from the geometric center in Figure 2 can be clearly seen in Figure 6. The velocities of the northern FMKs increase with radial distance, ranging from around 0 km s^{-1} at a $1'$ radius to around 1500 km s^{-1} at the outer edge ($3.5'$) of the sampled FMK distribution. The northern FMKs appear to trace a portion of an ellipse in the position-velocity plane, consistent with the kinematic signature of an expanding shell. Another identifiable property of the velocity distribution is that nearly all of the northern FMKs exhibit blueshifted emission, while, by contrast, the southern FMKs exhibit a more even mixture of blueshifted and redshifted emission.

It is also clear from Figure 6 that there is a significant spread in FMK radial velocities ($\sim 500\text{ km s}^{-1}$) at a given radius. This dispersion is much larger than the random statistical error in velocity ($\sim 50\text{ km s}^{-1}$). The FMKs may then not strictly lie on a geometrically thin shell, making the definition of a shell expansion radius less well defined. However, we can at least fit a velocity ellipsoid to the outermost FMKs in the position-velocity diagram in order to obtain a rough expansion age for G292.0+1.8.

We fit the position-velocity distribution in Figure 6 with a velocity ellipsoid, leaving the radius R_{ej} , expansion velocity V_{ej} and systemic velocity V_c as free parameters. The expansion center coordinates were fixed to those of the geometric radio center of GW03. Excluding the southernmost FMKs, we fit a curve to match the outermost points of the radial velocity distribution as closely as possible, paying particular attention to matching the most well-defined pattern, that of the blueshifted northern FMKs. Our best estimate is marked by the solid curve in Figure 6.

The fitted radius of the FMK position-velocity distribu-

tion is $3/4$ ($5.9 d_6$ pc). This defines a circle with northern edge lying just interior to the northernmost FMKs seen in Figure 1. We find an FMK shell velocity $V_{ej} = 1700 \text{ km s}^{-1}$, with a velocity centroid $V_c = +100 \text{ km s}^{-1}$, although the latter is not very tightly constrained since it is comparable to the random statistical error in FMK radial velocities ($\pm 50 \text{ km s}^{-1}$) and is smaller than the FMK velocity dispersion. Our derived systemic shift is substantially smaller than the shifts seen in the other known OSNRs: Cas A ($+900 \text{ km s}^{-1}$; Reed et al. 1995), N132D (-500 km s^{-1} ; Morse et al. 1995), E0102-72.3 (-500 km s^{-1} ; Tuohy & Dopita 1983), 0540-69.3 ($+370 \text{ km s}^{-1}$; Kirshner et al. 1989) and the remnant in NGC 4449 ($+500 \text{ km s}^{-1}$; Balick & Heckman 1978). Assuming free expansion of the shell, the age τ ($\equiv R_{ej}/V_{ej}$) is $3400 d_6$ years.

As a separate exercise, we also computed τ for two separate cases: (1) assuming the FMKs formed with a range of initial velocities but experienced negligible deceleration over the lifetime of the SNR, and (2) assuming the FMKs formed with identical velocities but with different knots experiencing differing degrees of deceleration over the lifetime of the SNR. In case 1 we fit the position-velocity distribution of all the FMKs, including the knots left out of the previous fit. In that case, we found a radius of $2'75$ ($4.8 d_6$ pc), a shell velocity of 1500 km s^{-1} and $V_c = +85 \text{ km s}^{-1}$ (this fit is marked by the dashed ellipse in Figure 6). These numbers give $\tau = 3100 d_6$ years. In case 2 we did not know the degree of deceleration of each individual knot, so we took the 500 km s^{-1} spread in the FMK velocity distribution as an approximation of the maximum deceleration experienced by the outermost knots. In that case, the original speed of the outermost knots was $V_0 = V_{ej} + \Delta V = 1700 + 500 = 2200 \text{ km s}^{-1}$, and the expression for the age is now $\tau \equiv R_{ej}/(V_0 - \frac{1}{2} \Delta V)$. Taking $R_{ej} = 3/4$ ($5.9 d_6$ pc), the resulting age is $\tau = 3000 d_6$ years. Thus, the range in ages derived from our analysis is $(3000-3400) d_6$ years.

The kinematic age derived from our analysis is nearly twice the value inferred by Murdin & Clark (1979) from spectroscopy of the spur. The disparity between our age and that of Murdin & Clark (1979) occurs because the expansion radius of the FMKs ($3/4$) is nearly 70% larger than that of the spur ($\sim 2'$), while the expansion velocities of the two distributions are nearly the same ($\sim \pm 1700 \text{ km s}^{-1}$). As we illustrate in the next section, the position-velocity diagram of the eastern spur is highly complex and structured. It is unclear whether a simple geometric expansion model can be applied to the spur; therefore, we believe that modeling the FMK kinematics provides cleaner, better estimates of both the expansion velocity and age of G292.0+1.8.

Recently Chevalier (2005) has applied self-similar models to constrain the supernova explosion types of a number of known core collapse SNRs, including G292.0+1.8. The models use observationally determined parameters such as the pulsar period and spindown rate, PWN luminosity and blast wave radius to classify the natal explosion type of each SNR. In the case of G292.0+1.8 assuming a distance of 6 kpc, Chevalier (2005) found that an age of 2700–3700

years was required for consistency with his models. Another estimate of the remnant's age, 2900 yrs, comes from the spindown age of the pulsar, PSR J1124-5916, associated with G292.0+1.8 (Camilo et al. 2002). These values are in good agreement with the age of $(3000-3400) d_6$ years from our fit to the FMK radial velocities in G292.0+1.8. This consistency in age estimates supports our assumption that the outermost knots in the position-velocity distribution have not been strongly decelerated.

6.2. THE SPUR

The position-velocity diagram of the spur (Figure 7) presents a far more complex kinematic picture than that of the FMKs (Figure 6). Although the spur does exhibit some of the overall properties expected from an expanding shell (e.g., the inward progression of the [O III] emission with increasing radial velocity seen in Figure 2), one is hard pressed to identify the kinematic signature of such a shell in Figure 7. One place where such a kinematic signature possibly appears is in the redshifted ejecta north of the expansion center. Between radii of $1'$ and $2'$, the velocity of this material monotonically decreases from $+1000 \text{ km s}^{-1}$ to 0 km s^{-1} . A more prominent feature is the tendency for many of the points in the position-velocity diagram to aggregate into radially extended clusters at nearly constant velocity. In particular, as demonstrated in Figure 7, there are two clusters of points (mostly toward the south) located at roughly 0 km s^{-1} and $+950 \text{ km s}^{-1}$ (both noted by Braun et al. (1983)⁵), with a similar but less distinct clustering possibly at -300 km s^{-1} . Braun et al. (1983) interpreted these features as 'breakouts' of O-rich clumps superimposed on a more uniform, expanding shell of ejecta. The RFP data appear to be consistent with this interpretation. Despite the rather confused radial velocity picture of the spur, both this feature and the FMK distribution described earlier extend over a total velocity range of approximately 3000 km s^{-1} .

PSR J1124-5916 in G292.0+1.8 is intriguingly close to the inner edge of the O-rich spur (marked in Figure 1). It is offset $\sim 45''$ eastward from the geometric center of the SNR, implying a substantial velocity component ($V_\perp \sim 450 \text{ km s}^{-1}$ for $\tau = 3400$ years) in the direction of the spur. This feature, combined with the known presence of a luminous PWN around PSR J1124-5916 raises an interesting question about the origin of the spur emission: could the spur be a shell of dense ejecta swept up from the inside by the motion of PSR J1124-5916?

There have been no unambiguous kinematic signatures predicted for the interaction between a PWN and SN ejecta. However, vital clues may be found in existing optical spectra of this OSNR: we would expect that as PSR J1124-5916 moved through the interior of G292.0+1.8 the innermost ejecta (mostly Ar-Fe produced in explosive nucleosynthesis) would be the first material to be shocked by the PWN. The lack of line emission from elements heavier than S in the global optical spectra of G292.0+1.8 (Murdin & Clark 1979; Sutherland & Dopita 1995; WL05) strongly indicates that the optical emission from the spur does not arise in a PWN/O-rich ejecta interaction. As mentioned earlier, X-ray emission from these heavier species is also absent in the *Chandra* spectra of

⁵Braun et al. (1983) employs the word 'spur' to describe only the radially extended, constant velocity features traced in the optical spectra, whereas we use the word as a descriptive term for the morphology of the O-rich material.

the G292.0+1.8 ejecta (Park et al. 2004), suggesting that in general there has been little or no interaction between the PWN and SN ejecta. A strong contrast may be drawn between here and the case of the OSNR 0540–69.3 in the LMC, where the PWN observed in the X-rays is completely enclosed by a ring of [O III]-emitting ejecta (Reynolds 1985). There, optical emission from S, Ar, Fe and Ni are observed in addition to the usual O and Ne lines (Kirshner et al. 1989; Serafimovich et al. 2004). Based on evolutionary considerations, Reynolds (1985) ascribed the optical emission from 0540–69.3 to a PWN/ejecta interaction, consistent with the presence of optical emission from the innermost ejecta.

The remaining interpretation for the spur emission in G292.0+1.8 is that it arises in an overdense shell of ejecta overtaken by the reverse shock. Evidence for this picture may be found by comparing the morphology of the spur with HST optical images of Cas A (Fesen et al. 2001), the most well-studied OSNR. Although the size scales of the Cas A and G292.0+1.8 filaments differ by over an order of magnitude, they bear a striking similarity: both follow a concave shape, curving away from the SNR expansion center, and both exhibit the scalloped morphology characteristic of Rayleigh-Taylor instabilities (Figure 8). Most importantly, the ‘wiggles’ in the spur point away from the expansion center, in close analogy to similar features seen in Cas A. This suggests that high density material is penetrating into overpressurized, less dense material, precisely the condition required to produce Rayleigh-Taylor instabilities. These instabilities would likely leave a significant kinematic imprint on the ejecta velocity distribution, and may be partly responsible for much of the dispersion seen in the position-velocity diagram of the spur (Figure 7).

7. LOW VELOCITY OPTICAL EMISSION

7.1. $H\alpha$ EMISSION

After following the procedure described earlier for subtracting stars from the RFP scans, we examined the $H\alpha$ datacube for evidence of hydrogen and nitrogen line emission from G292.0+1.8. The only scans exhibiting structure were the zero velocity scan and its two adjacent frames centered on -62 km s^{-1} and $+85 \text{ km s}^{-1}$. Interpolating the flux between RFP frames, we produced an image of the entire field at zero radial velocity. In Figure 9 the continuum-subtracted zero velocity $H\alpha$ image is shown along with contours from the zero-velocity [O III] image. Overall there is very little detailed correspondence between the $H\alpha$ and [O III] morphologies of G292.0+1.8. In particular, the high-velocity [O III] structures observed at all velocities in the RFP images exhibit little or no corresponding $H\alpha$ emission.

The most prominent features in the $H\alpha$ image are a set of narrow filaments $30''$ – $40''$ in length seen mostly on the eastern half of the $H\alpha$ image. The filaments lie close to the O-rich spur, but due to the grossly dissimilar morphologies of the $H\alpha$ and [O III] emissions, it is unlikely that they trace the same material. The filaments appear at zero radial velocity (i.e., in the rest frame of G292.0+1.8), which raises the possibility that they are clouds of either shock-excited or photoionized circumstellar material. The lack of obvious emission from these filaments in both the [O III] RFP scans and the *Chandra* image of G292.0+1.8 places

a strong constraint on the excitation mechanism of the $H\alpha$ filaments: we can rule out both radiative shocks in O-rich material and radiative shocks faster than 100 km s^{-1} in ISM material (Hartigan, Raymond & Hartmann 1987).

If the filament emission is produced in slow ($< 100 \text{ km s}^{-1}$) radiative shocks, then we should be able to match the [N II]: $H\alpha$ flux ratios with the theoretically predicted values. We obtained a spectrum from one of the filaments (the extraction box is marked in Figure 9 and the spectrum is plotted in Figure 10) and fit the $H\alpha$ and [N II] $\lambda 6548$ line profiles. Both lines were fit by Voigt profiles with widths fixed at the instrumental values. To within the errors ($\pm 15 \text{ km s}^{-1}$) the $H\alpha$ and [N II] $\lambda 6548$ lines are centered on zero radial velocity, consistent with an origin in the circumstellar medium around G292.0+1.8.

From the profile fits we find that the ratio [N II]($\lambda 6548$): $H\alpha \approx 0.2$, with spectra extracted from the other nearby filaments exhibiting nearly the same ratios. Theoretical values of the [N II]($\lambda 6548$): $H\alpha$ ratio have been calculated by Hartigan, Raymond & Hartmann (1987) for plane parallel shocks with equilibrium preionization and cosmic abundances. The ratios range from approximately 0.1 for a 90 km s^{-1} shock (higher values can be rejected because [O III] emission turns on very rapidly for faster shock speeds) down to nearly zero for a shock speed of 20 km s^{-1} . For this scenario to be correct, we therefore require significant enhancement (by factors of 2 or more) in the nitrogen abundance in the ambient medium. This explanation also requires very high densities in the emitting filaments. The shock parameters of the G292.0+1.8 blast wave ($n_0 \sim 1 \text{ cm}^{-3}$, $V_S \sim 2000 \text{ km s}^{-1}$; GW03) imply a high ram pressure, which combined with pressure conservation and low shock speed in the filaments ($\lesssim 90 \text{ km s}^{-1}$) results in predicted preshock cloud densities $\gtrsim 100 \text{ cm}^{-3}$. The presence of such dense, localized structures in a predominantly low density medium seems unlikely, but it may be possible if the progenitor wind was highly clumped.

An alternate explanation for the filaments is that they are low density ($n \sim 1 \text{ cm}^{-3}$), neutral clouds photoionized by radiation from the shocks in G292.0+1.8. As noted by Hamilton & Fesen (1986) for SN 1006 and Morse et al. (1996) for N132D, the shocked metal-rich ejecta inside a supernova remnant is a source of hard UV and X-ray line radiation which escapes out into the ISM and ionizes material surrounding the SNR. Another source of hard radiation is He II $\lambda 304$ photons from the ISM material swept up by the blast wave. Exposed to the dilute, time varying radiation field of the SNR, nearby H I clouds could remain significantly neutral while being heated to temperatures $\sim 12,000$ – $15,000 \text{ K}$ (Ghavamian et al. 2000). The resulting optical emission from the cloud would feature faint $H\alpha$, [N II], [S II] and $H\beta$ emission and almost negligible [O III] (as seen in Tycho’s SNR, Ghavamian et al. 2000). Unlike the case of radiative shocks, the photoionization scenario can produce the observed [N II]: $H\alpha$ ratios without the need for enhancing the nitrogen abundances in the emitting clouds. A long-slit spectrum with larger wavelength coverage and higher spectral resolution is required to definitively establish the physical properties of the filaments in Figure 10 and to decide between the photoionization and radiative shock scenarios.

As we have already mentioned, there is an absence of

high-velocity $H\alpha$ and $[N\ II]$ emission over the dynamical range sampled by our RFP data. This sort of material has been seen in Cas A (the ‘fast-moving flocculi’, or FMFs, reported in Fesen, Becker & Blair (1987)). The Cas A FMFs exhibit properties similar to both FMKs and QSFs, namely high velocities and emission from nitrogen, hydrogen and helium. They are believed to be fragments of the progenitor photosphere which were expelled at high velocity during the supernova explosion. Since the photosphere comprises the outermost layer of the ejecta, it is the first material to be overrun by the reverse shock. G292.0+1.8 is nearly ten times older than Cas A, while the survival time of dense, shocked knots is typically only on the order of a few decades. It seems likely then that any hydrogen/nitrogen-rich material ejected from the surface of the progenitor star would have been overrun and destroyed at an earlier evolutionary phase of G292.0+1.8.

7.2. OPTICAL EMISSION FROM THE EQUATORIAL BAR

In our optical investigation of G292.0+1.8 it is perhaps our study of the equatorial belt that benefits the most from the kinematic resolving power of the RFP. As previously defined (see §4), the equatorial belt appears in the zero radial velocity $[O\ III]$ image as a narrow bar of emission elongated in the E-W direction. This is very different from the larger, clumpier structure seen in the narrowband image in Figure 1 due to the geometric projection of high velocity knots (such as K1 and K2 in Figure 1) onto the zero-velocity bar.

We can trace the detailed structure of the belt at zero velocity using the marked features in Figure 11. In this image the most prominent portion of the bar (B1) lies immediately west of the radio geometric center and is approximately $5''$ thick and $22''$ long. The $[O\ III]$ surface brightness of B1 is $\sim 20\%$ of the brightest emission in the $[O\ III]$ spur. Fainter bar emission can also be seen extending to the east (B2) and southeast (B3) of B1. Both the bar and a patchy feature $2'$ further southwest (marked as P1 in the figure) are visible in our $H\alpha$ image, although the bar is relatively fainter and smoother in $H\alpha$ than in $[O\ III]$. As we will show in Section 8.2, features B1 and B2 appear to be optical counterparts to portions of the X-ray bar seen first in the *Einstein* and then the *Chandra* image of G292.0+1.8. On the other hand, another prominent zero-velocity feature seen in Figure 11, B3, does not exhibit a clear X-ray counterpart.

8. COMPARING THE X-RAY, OPTICAL, AND RADIO EMISSION FROM G292.0+1.8

The RFP data of G292.0+1.8 shows that the $[O\ III]$ emission is distributed over a wide range in velocity and consists of multiple components. Therefore, to understand the interaction of G292.0+1.8 with its surrounding medium we must separate the ejecta knot $[O\ III]$ emission from circumstellar/ambient $[O\ III]$ emission. Since much of the emission from G292.0+1.8 is emitted in the X-ray band, comparing our RFP data with the spectacular *Chandra* ACIS image of G292.0+1.8 provides a link between the optically-emitting components and global variations in density, temperature, composition and ionization state. For this comparison we utilized a 38 ks archival *Chandra* observation of G292.0+1.8, filtered to include only the oxy-

gen K line emission between 0.55 and 0.75 keV. We then smoothed the image with a boxcar of variable size, preserving a minimum S/N of 3 per smoothing beam. The smoothed 0.55–0.75 keV image of G292.0+1.8 is shown in the left panel of Figure 12. The X-ray contours are also shown to provide a reference for the eye in distinguishing contours around emission minima from contours around emission maxima. Contours of the 0.55–0.75 emission are overlaid onto the zero velocity $[O\ III]$ and $H\alpha$ images in the middle and right panels, respectively.

8.1. TRACING THE EJECTA DISTRIBUTION

An important question arising from our RFP analysis is how the fast-moving ejecta seen in $[O\ III]$ correlate with the chaotic X-ray emitting material seen in the *Chandra* ACIS image of G292.0+1.8. The answer appears to depend on whether the optical emission in question belongs to the FMK population, equatorial belt or eastern spur material. In the following discussion, we present a qualitative first comparison between the optical and X-ray ejecta emission in G292.0+1.8.

FMKs – There is a clear spatial correlation between some FMKs seen in the $[O\ III]$ RFP data of G292.0+1.8 and the knots of X-ray ejecta seen in the *Chandra* image (Figure 13). In particular, at the positions of the northern (blueshifted) knots, the extended X-ray features invisible at optical wavelengths often appear to terminate in FMKs of $[O\ III]$ emission lacking X-ray counterparts. In addition, some of the $[O\ III]$ FMKs appear to be ‘nested’ at intersection points between elongated strands of X-ray-emitting ejecta.

The correlations described above are consistent with ram pressure conservation in ejecta fragments of variable density. When an ejecta fragment encounters the overpressured gas behind the reverse shock, there are radiative shocks ($V_S \sim 100\text{--}200\text{ km s}^{-1}$) driven into the densest portions of the clump ($n \gtrsim 100\text{ cm}^{-3}$), while partially radiative shocks ($V_S \sim 500\text{ km s}^{-1}$) form in locations of intermediate density ($n \sim 10\text{ cm}^{-3}$) and fast non-radiative shocks ($V_S \gtrsim 1000\text{ km s}^{-1}$) form in least dense ($n \lesssim 1\text{ cm}^{-3}$) portions of the clump. In the resulting mixture of conditions, the brightest optical and X-ray features often follow mutually exclusive spatial distributions, while material of intermediate surface brightness are often detected in both bands.

Whereas in a number of northern FMKs we can trace what appear to be connected strands of ejecta material between the optical and X-ray images, most of the southern FMKs tend to appear as solitary localized structures in $[O\ III]$ surrounded by more extended, diffuse X-ray emission (Figure 13). The dissimilarity in the X-ray-optical correlation between the northern and southern FMKs may reflect a comparatively larger density contrast in the southern ejecta distribution: most of the southern knots may be composed of material too dense to produce anything but radiative shocks. It is unclear whether this inference, if correct, points to variations in the pattern of hydrodynamical instabilities during the SN event or whether it reflects differences between the history of the reverse shock/ejecta interaction in the northern and southern portions of G292.0+1.8.

A large density contrast between the optically emitting

and X-ray emitting material in the southern FMKs would have consequences on the morphology and kinematics of the knots. Using hydrodynamical simulations, Klein, McKee & Colella (1994) and Jones, Kang & Tregillis (1994) showed that among the knots interacting with the low density ambient medium, those with a large density contrast parameter χ ($\equiv \rho_{\text{knot}}/\rho_{\text{amb}}$) remain intact and undecelerated longer than knots with smaller contrast parameters. Anderson et al. (1994) found that reverse-shocked knots follow roughly a three-phase evolutionary process: (1) a bow shock phase, where the knot drives a shock into the low density medium ahead of it and in the process is itself compressed by a reverse shock, (2) an instability phase where the reverse shock exits the back side of the knot and a series of Rayleigh-Taylor and Kelvin-Helmholtz instabilities are initiated, and (3) a dispersal phase where the knot is strongly decelerated and the instabilities shred the structure into smaller pieces. Anderson et al. (1994) noted that in a given knot the optical emission from radiative shocks will cease once the shock emerges from the rear of the knot.

The FMKs seen in [O III] have not been significantly decelerated (see §6.1), so we can safely conclude that these knots have not yet reached the third (dispersal) phase of evolution. On the other hand, Jones, Kang & Rudnick (1994) predict that the nonthermal radio emission from a knot will rise sharply during the second (instability) phase, as shearing forces amplify magnetic fields near the boundary of the knot. Comparing the [O III] image with the 20 cm continuum image of GW03, we find that some FMK groups, such as the two northernmost groups seen in Figure 1, are correlated with obvious patches of enhanced radio emission (Figure 14). In contrast, other FMKs, such as the southernmost group of elongated knots in Figure 1, show little associated radio continuum emission (Figure 14).

The presence of both optical and radio emission from the FMKs suggests that the knots are somewhere between the bow-shock and instability phases of evolution. We note that the northernmost knots should be further into the instability phase than the southern knots, because of the greater relative prominence of radio emission from the northern knots. Again, a higher density contrast for the southern knots would be consistent with this scenario. Since it is rare to detect X-ray, optical, and radio emission from isolated fragments of ejecta in young SNRs, further multiwavelength studies are clearly warranted. However, these are beyond the scope of the current article and are left to future work.

The Spur – The most coherent ejecta structure seen in [O III] images of G292.0+1.8 shows little morphological correlation with features detected in the *Chandra* image. As shown in the middle panel of Figure 12, the top portion of the crescent-shaped spur is seen at zero velocity, at the eastern end of the equatorial bar structure. The top of the spur does not match any bright features in the *Chandra* image. The lower portion of the spur (the redshifted structure seen out to $+1700 \text{ km s}^{-1}$ in Figure 2) also shows little obvious X-ray emission. This suggests that virtually all of the main spur is composed of dense O-rich material. However, the streamers of material running southward of the spur exhibit [O III] clumps that lie at tips of X-ray knots. This may indicate that the ejecta ma-

terial in the streamers is of more variable density, similar to what is seen in the FMKs.

8.2. COMPARING THE OPTICAL AND X-RAY EMISSION FROM THE EQUATORIAL BAR

The equatorial X-ray bar is perhaps the most prominent feature in the broadband X-ray image of G292.0+1.8. When this feature was first discovered in the *Einstein* image, it was unclear whether the emission was from ejecta or circumstellar material. After finding that the kinematics of the [O III] emission in 1E 0102.2–7219 could be explained by expansion of a distorted ring of high velocity ejecta, Tuohy & Dopita (1983) suggested that the equatorial belt seen in the *Einstein* image of G292.0+1.8 could be a similar structure seen nearly edge-on. However, detailed spectral analyses of the *Chandra* X-ray data (Park et al. 2002, 2004; Gonzalez & Safi-Harb 2003) cast doubt on this interpretation when these studies showed that the composition of the bar was generally consistent with cosmic abundances.

A comparison of the optical and X-ray images in Figure 12 indicates that the zero-velocity features B1 and B2 making up the [O III] bar are likely the optical counterparts of some parts of the X-ray structure seen by Park et al. (2002). The gap in the bar is closely matched in both the [O III] and X-ray images. In addition to the belt, a circular patch of [O III] emission $35''$ across can be seen approximately $1.3'$ southwest of B1 (feature P1 in Figure 1). In the X-ray image P1 lies at the end of a ridge of material extending out from the center toward the southwest, suggesting that they are part of the same structure. Some features such as B3 (Figure 11) are more difficult to interpret since they appear to be circumstellar material (are seen only at zero radial velocity), but exhibit no clearly associated H α or X-ray emission.

Other than these cases, finding direct matches between H α and X-ray features in G292.0+1.8 is less straightforward. The X-ray emission and zero velocity H α emission in Figure 12 show little spatial correlation. As mentioned earlier, there is no X-ray emission from the H α filaments on the eastern side of the remnant, indicating that they are not fast, non-radiative shocks in neutral gas (i.e., Balmer-dominated shocks, Chevalier & Kirshner 1978, Chevalier, Kirshner & Raymond 1980).

The most plausible explanation for the equatorial bar emission in [O III], H α and X-rays is that it is produced by partially radiative shocks (i.e., shocks with incomplete cooling zones) in moderate density ($n \sim 10 \text{ cm}^{-3}$) circumstellar material. The incomplete cooling zones occur when the shock front has been moving through material for a time comparable to, but less than the cooling time scale of the shocked gas. Features B1, B2 and P1 in G292.0+1.8 may be the sites of partially radiative shocks in cosmic abundance material.

Partially radiative shocks have been modeled for the case of the Cygnus Loop by Raymond et al. (1988), who showed that the relative flux of [O III] to H β (or H α) is determined by the column density where the postshock flow terminates. Therefore, if the shock is viewed at a time before the cooling zone has fully formed, it is possible for the output [O III] flux to significantly exceed that of both H β and H α . A truncated cooling zone in the equatorial bar would also explain its overall optical faintness, since

the emitting gas would not have reached the full compression (~ 100) attainable in a fully radiative shock. The best way to confirm the existence of a partially radiative shock would be to measure such ratios as $[\text{O III}]:\text{H}\beta$, $[\text{O II}]/\text{H}\beta$ and $[\text{O I}]:\text{H}\alpha$ from a long-slit spectrum of the bar and to compare the results with numerical shock model predictions. This will be the focus of a future study.

9. SUMMARY

Clearly, G292.0+1.8 exhibits a very complex morphology. The optical study of WL05 and our RFP kinematic investigation have only begun to reveal the rich variations in elemental abundances, densities and kinematic properties across this OSNR. We believe that further study will ultimately prove G292.0+1.8 to be every bit as interesting as Cas A. From Rutgers Fabry-Perot data we have extracted and fit $[\text{O III}] \lambda 5007$ line profiles to 524 regions in G292.0+1.8. Our main results are as follows:

1. The detection of numerous fast-moving knots of O-rich ejecta. These FMKs are similar to the localized knots of ejecta seen in Cas A. An interesting property of the FMKs is that very few are detected at redshifted velocities; either the O-rich ejecta are preferentially distributed on the near side of G292.0+1.8 or the reverse shock has not yet encountered all the ejecta on the far side of the remnant. The position-velocity diagram of the FMKs exhibits the unmistakable kinematic signature of an expanding shell expanding at a radial velocity of 1700 km s^{-1} . Assuming a distance of 6 kpc, we derive an expansion age of 3000–3400 years for G292.0+1.8. Our fits indicate that the centroid of the FMK velocity distribution is only slightly redshifted ($\sim +100 \text{ km s}^{-1}$). This systemic shift is substantially smaller than the shifts seen in the other known OSNRs, and may reflect a difference in explosion asymmetry between G292.0+1.8 and other OSNRs.

2. The bright spur of O-rich material which dominates the optical appearance of G292.0+1.8 is kinematically resolved into a rippled shell of predominantly redshifted ejecta. However, interpreting the position-velocity diagram of the spur is not straightforward. Extracting spectra from a grid of regions covering the face of the spur, we find that some points in the position-velocity diagram tend to aggregate into groups of constant velocity. These features are seen at -300 km s^{-1} , 0 km s^{-1} and $+950 \text{ km s}^{-1}$, and we interpret them as ejecta clumps that have broken away from the main redshifted shell of expanding material. Morphologically, the wiggles seen in the spur material at high redshifted velocities ($\geq 600 \text{ km s}^{-1}$) are

similar to the Rayleigh-Taylor unstable structures seen in Cas A. As in Cas A, the wiggles in the spur of G292.0+1.8 point away from the expansion center, indicating that the instabilities arise in reverse-shocked ejecta. This argues against the possibility that the spur is ejecta swept from the inside out by the relativistic wind nebula of the nearby pulsar PSR J1124–5916.

3. Optical detection of an equatorial bar matching portions of the bright X-ray bar structure seen in prior *Einstein* and *Chandra* images of G292.0+1.8. The bar is detected at the systemic radial velocity of G292.0+1.8 (0 km s^{-1} , or $V_{LSR} = 4.5 \text{ km s}^{-1}$) in both $[\text{O III}]$ and $\text{H}\alpha$. The optical emission is faint, suggesting that the shocks driven into this material are just now becoming radiative. There are several other structures near the bar, but not aligned with it, which exhibit faint $[\text{O III}]$ and $\text{H}\alpha$ but are bright in X-rays. Our detection of the bar in both $[\text{O III}]$ and $\text{H}\alpha$ confirms the assertion by Park et al. (2002, 2004) and Gonzalez & Safi Harb (2003) that this material is of cosmic composition. The bar may be portion of a ring of circumstellar material similar to what is seen in SN 1987A, but with the difference that it is nearly an order of magnitude larger and of much lower density. There are a number of FMKs along the line of sight to the belt that are kinematically resolved in our RFP scans but which give a stranded, chaotic appearance to this region in the narrowband $[\text{O III}]$ images (WL05).

There appears to be an absence of fully radiative shocks in cosmic composition material in G292.0+1.8. All observed shocks are either fully non-radiative or partially radiative. From our RFP spectra we are unable to determine with certainty whether the belt is enhanced in nitrogen as may be expected for a circumstellar wind. Deep long-slit spectroscopy and detailed modeling will be required to settle this issue.

P. G. would like to thank John Raymond for helpful discussions on the shock physics presented in this paper, P. F. Winkler for permission to use the narrowband $[\text{O III}]$ image of G292.0+1.8 and Bryan Gaensler for making the 20 cm radio image available. The authors would also like to thank the referee for very helpful suggestions on clarifying the science of the paper and improving the presentation. This work was partially supported by Chandra Grants GO0-1035X and GO1-2052X, and NSF grant AST 9619510. J. P. H. and T. B. W. would like to thank the staff of CTIO for their hospitality and support during the Fabry-Perot observations.

REFERENCES

- Anderson, M. C., Jones, T. W., Rudnick, L., Tregillis, I. L. & Kang, H. 1994, *ApJ*, 421, L31
 Balick, B. & Heckman, T. 1978, *ApJ*, 226, L7
 Blair, W. P., Kirshner, R. P. & Winkler, R. P. 1983, *ApJ*, 279, 708
 Blair, W. P., et al. 2000, *ApJ*, 537, 667
 Braun, R., Goss, W. M., Danziger, I. J. & Boksenberg, A. 1983, *IAUS* 101, 159
 Braun, R., Goss, W. M., Caswell, J. L. & Roger, R. S. 1986, *A&A*, 162, 259
 Camilo, F., et al. 2002, *ApJ*, 567, L71
 Chevalier, R. A. & Kirshner, R. P. 1978, *ApJ*, 219, 931
 ——— 1979, *ApJ*, 233, 154
 Chevalier, R. A., Kirshner, R. P. & Raymond, J. C. 1980, *ApJ*, 235, 186
 Chevalier, R. A. 2005, *ApJ*, 619, 839
 Clark, D. H., Tuohy, I. R. & Becker, R. H. 1980, *MNRAS*, 193, 129
 Dopita, M. A., Tuohy, I. R. & Mathewson, D. S. 1981, *ApJ*, 248, L105
 Fesen, R. A., Becker, R. H. & Blair, W. P. 1987, *ApJ*, 313, 378
 Fesen, R. A. et al., 2001, *AJ*, 122, 2644
 Gaensler, B. M. & Wallace, B. J. 2003 (GW03), *ApJ*, 594, 326
 Ghavamian, P., Raymond, J., Hartigan, P. & Blair, W. P. 2000, *ApJ*, 535, 266
 Gonzalez, M. & Safi-Harb, S., 2003, *ApJ*, 583, L94
 Goss, W. M., Shaver, P. A., Zealey, W. J., Murdin, P. & Clark, D. H. 1979, *MNRAS*, 188, 357
 Hartigan, P. M., Raymond, J. C. & Hartmann, L. 1987, *ApJ*, 316, 323
 Hughes, J. P. & Singh, K. P. 1994, *ApJ*, 422, 126
 Hughes, J. P., et al. 2001, *ApJ*, 559, L153
 Hughes, J. P., et al. 2003, *ApJ*, 591, L139
 Jones, T. W., Kang, H. & Tregillis, I. L. 1994, *ApJ*, 432, 194

- Kirshner, R. P., Morse, J. A., Winkler, P. F. & Blair, W. P. 1989, *ApJ*, 342, 260
- Klein, R. I., McKee, C. F. & Colella, P. 1994, *ApJ*, 420, 213
- Lasker, B. M. 1978, *ApJ* 223, 109
- Lasker, B. M. 1980, *ApJ* 237, 765
- Lawrence, S. S. et al., 1995, *AJ*, 109, 2635
- Lockhart, I. A., Goss, W. M., Caswell, J. L. & McAdam, W. B. 1977, *MNRAS*, 179, 147
- Mills, B. Y., Slee, O. B. & Hill, E. R. 1961, *Au. J. Phys.* 279, 708
- Minkowski, R., 1957, in *IAU Symp. 4, Radio Astronomy*, ed. H. C. van de Hulst (Cambridge: Cambridge Univ. Press), 107
- Morse, J. A., Winkler, P. F. & Kirshner, R. P. 1995, *AJ*, 109, 2104
- Morse, J. A., et al. 1996, *AJ*, 11, 509
- Murdin, P. & Clark, D. H. 1979, *MNRAS* 189, 501
- Park, S., et al. 2002, *ApJ*, 564, L39
- Park, S., et al. 2004, *ApJ* 602, L33
- Raymond, J. C., Hester, J. J., Cox, D., Blair, W. P., Fesen, R. A. & Gull, T. R. 1988, *ApJ*, 324, 869
- Reed, J. E., Hester, J. J., Fabian, A. C. & Winkler, P. F. 1995, *ApJ*, 440, 707
- Reynolds, S. P. 1985, *ApJ* 291, 152
- Serafimovich, N. I., Shibano, Yu. A., Lundqvist, P. & Sollerman, J. 2004, *A&A*, 425, 1041
- Sutherland, R. S. & Dopita, M. A. 1995, *ApJ*, 439, 365
- Tuohy, I. R., Clark, D. H. & Burton, W. M. 1982, *ApJ*, 260, 65
- Tuohy, I. R. & Dopita, M. A. 1983, *ApJ* 268, L11
- van den Bergh, S. 1979, *ApJ*, 234, 493
- Winkler, P. F. & Kirshner, R. P. 1985, *ApJ* 299, 981
- Winkler, P. F. & Long, K. S. 2005, *ApJ*, in preparation (WL05)

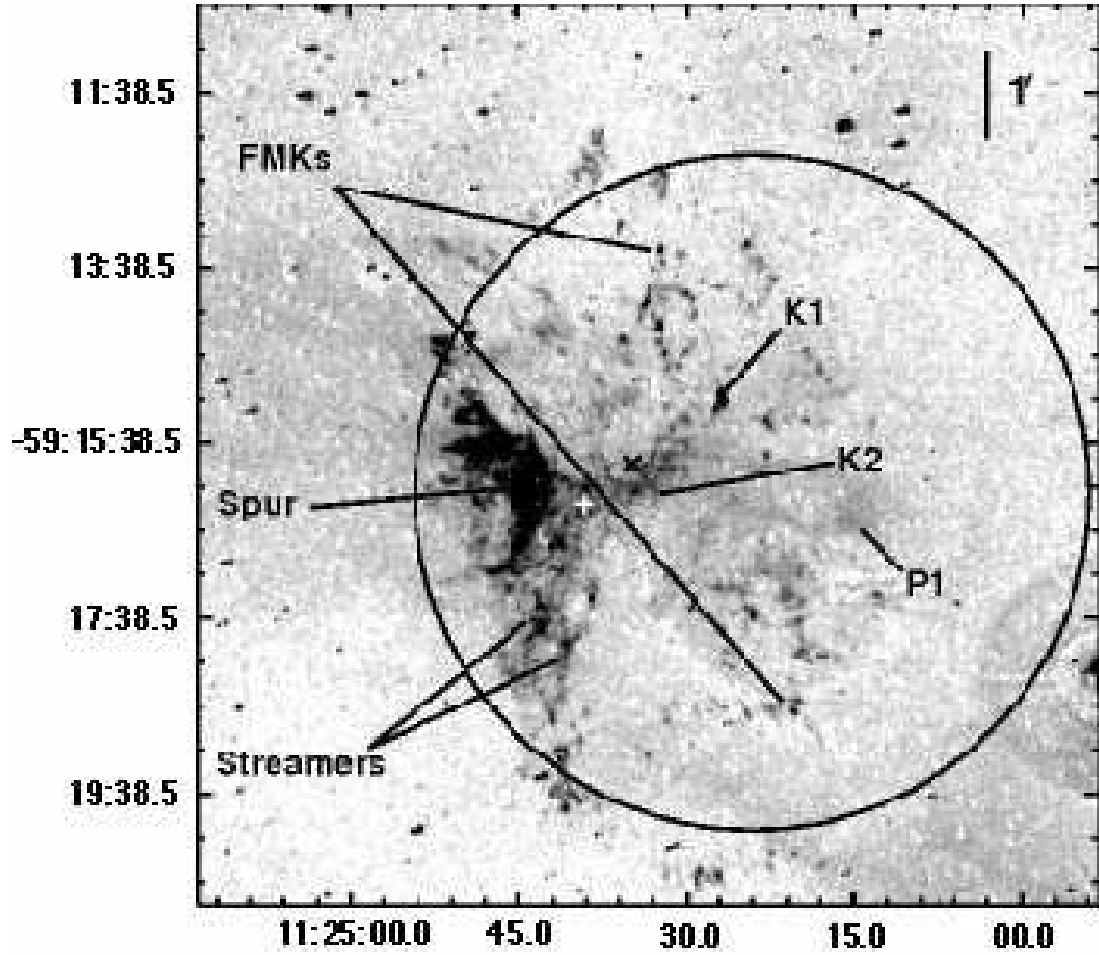


FIG. 1.— Continuum-subtracted narrow band [O III] image of G292.0+1.8 (WL05), showing the optical emission sampled by the RFP observations. The field of view of the RFP scans is marked by the solid black circle. The radio-derived geometric center for G292.0+1.8 (GW03) is marked by the ‘X’ and the location of the X-ray pulsar (Hughes et al. 2003) is marked by the crosspoint. Features discussed in the text are marked. N is at the top of each frame and E lies to the left. A full resolution figure can be found at <http://fuse.pha.jhu.edu/~parviz/papers/g292>.

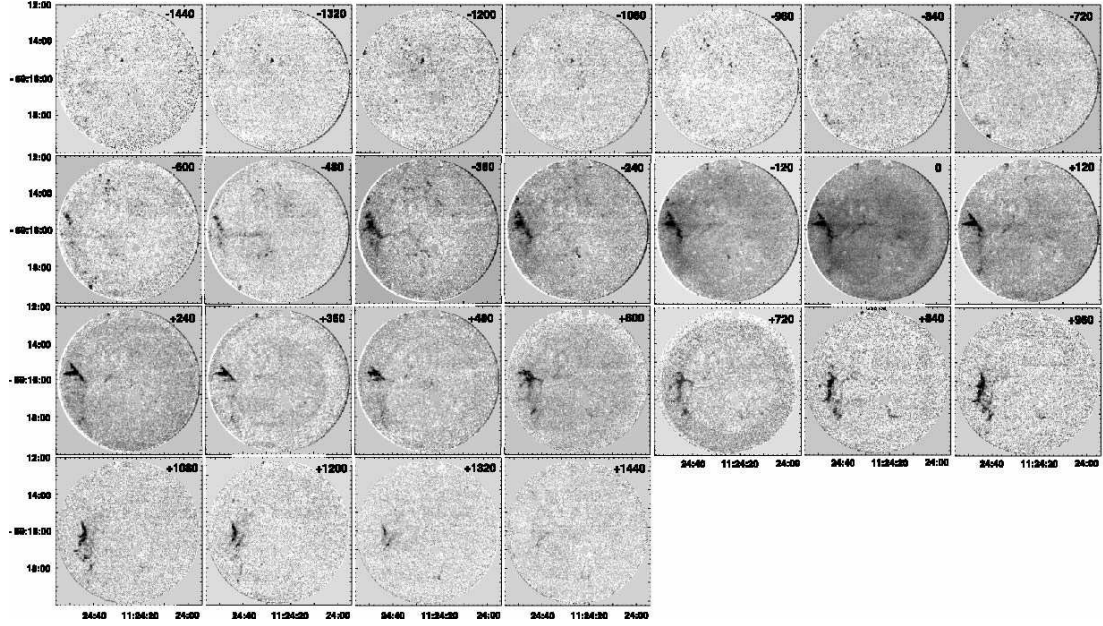


FIG. 2.— Continuum-subtracted [O III] scans of G292.0+1.8 flattened to show the entire SNR at a sequence of constant velocity slices. The radial velocity from rest is recorded in the upper right corner of each image. Residuals from stellar subtraction have been masked by interpolating over the surrounding background. The equatorial bar and a significant portion of the eastern O-rich spur are clearly seen in the zero velocity image, along with widespread diffuse [O III]. Fast-moving knots (FMKs) are seen mostly in the north above the bar. N is at the top of each frame and E lies to the left. The field of view of each image is $7''.8$. A full resolution figure can be found at <http://fuse.pha.jhu.edu/~parviz/papers/g292>.

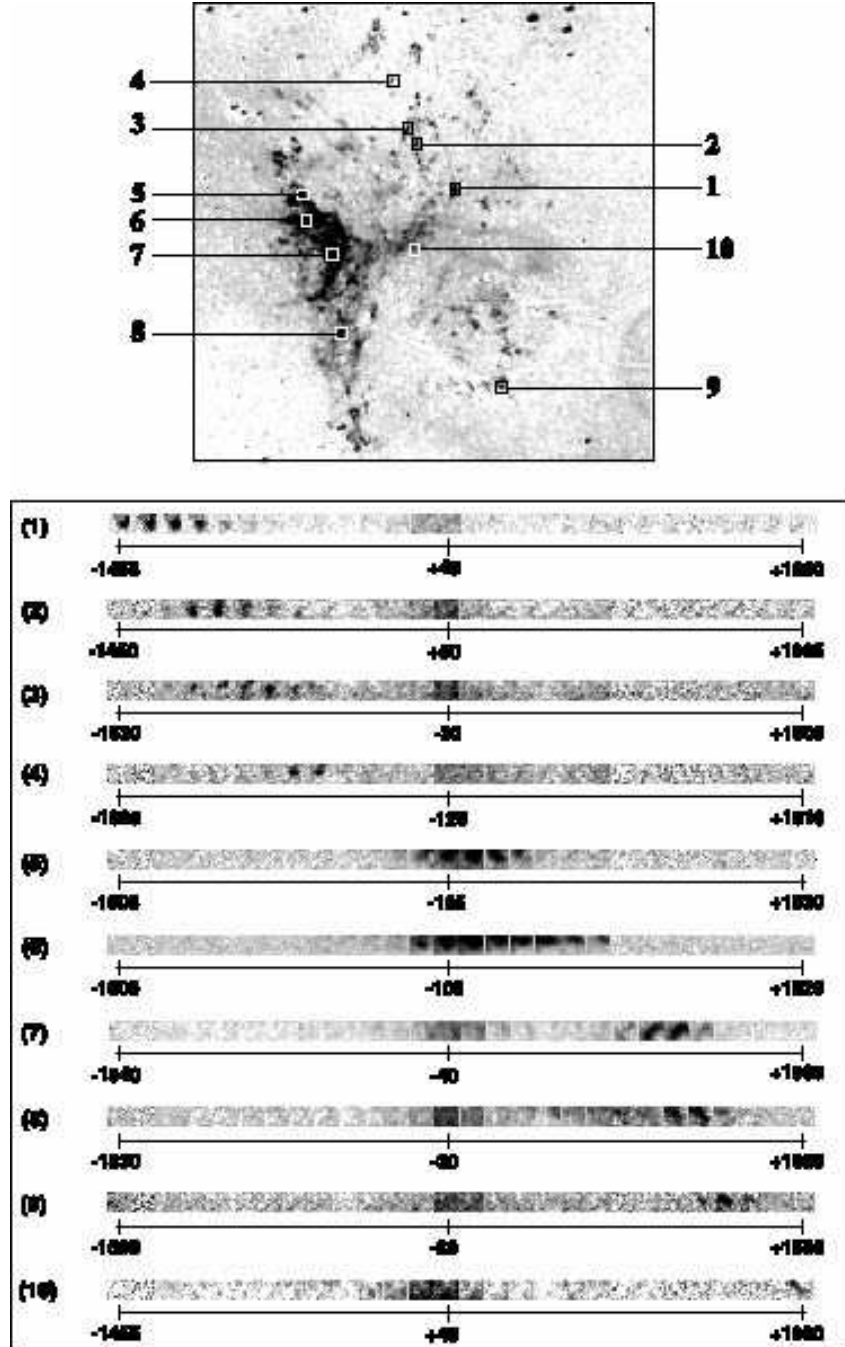


FIG. 3.— The bottom panel shows a sequence of ejecta knot images from the RFP data in the light of [O III] arranged side-by-side in velocity. The extraction regions are marked on the narrowband image of G292.0+1.8 from WL05 (top panel). Each square window in the bottom panel is $11'' \times 11''$ in size and the individual frames are separated by approximately 120 km s^{-1} in velocity. Radial velocities are marked at the bottom of each frame. A full resolution figure can be found at <http://fuse.pha.jhu.edu/~parviz/papers/g292>.

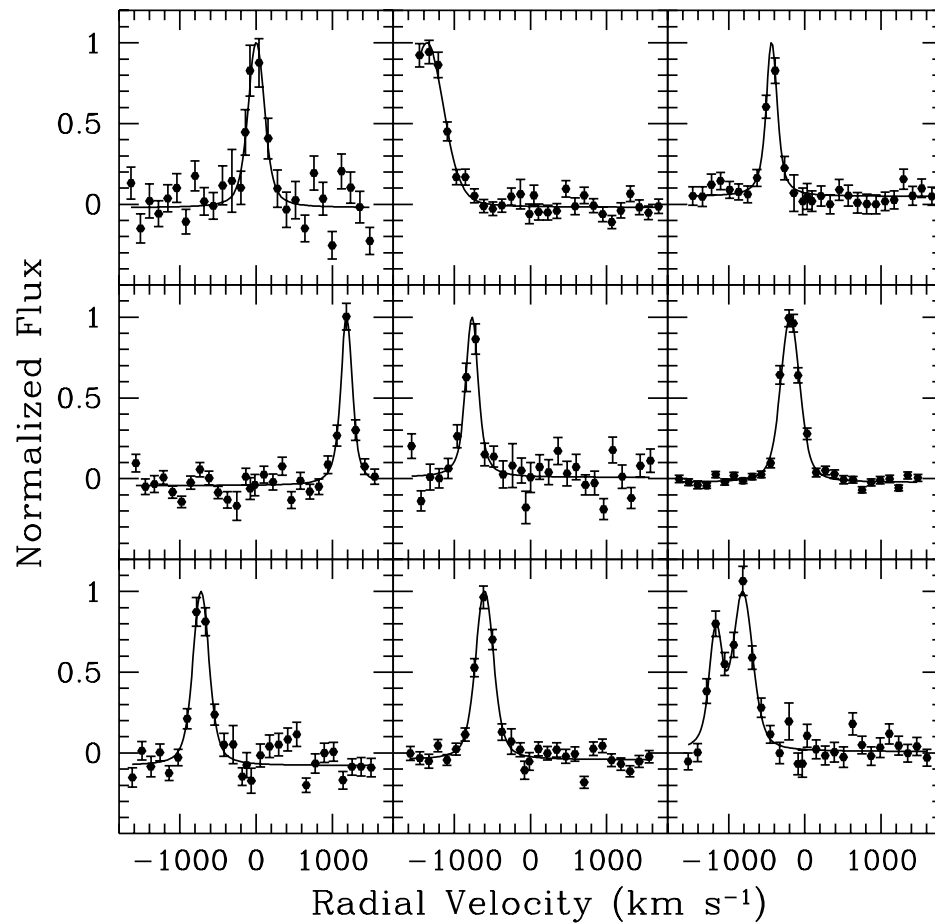


FIG. 4.— The [O III] profiles of 9 selected FMKs in G292.0+1.8. The solid line drawn through the data is the best fit to the line profile. Line profiles are shown over the full range of velocity shifts and include both low and high S/N examples.

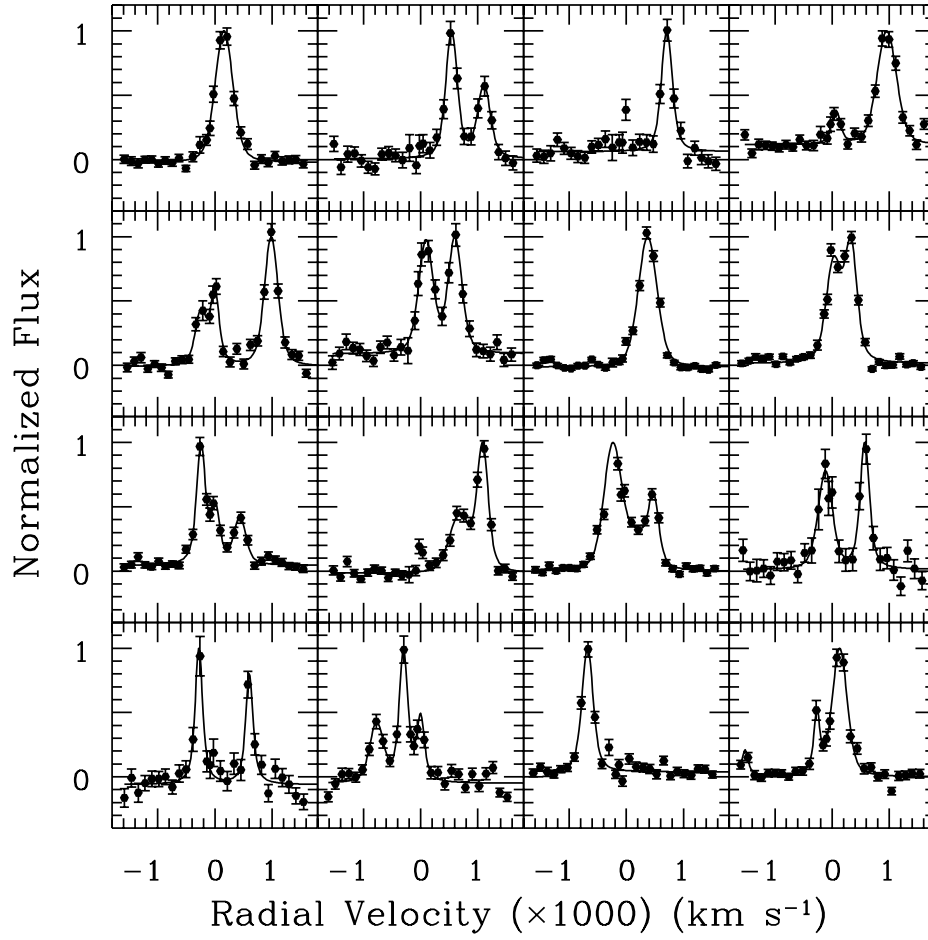


FIG. 5.— The [O III] profiles of 16 selected locations in the bright eastern spur region. The solid line drawn through the data is the best fit to the line profile.

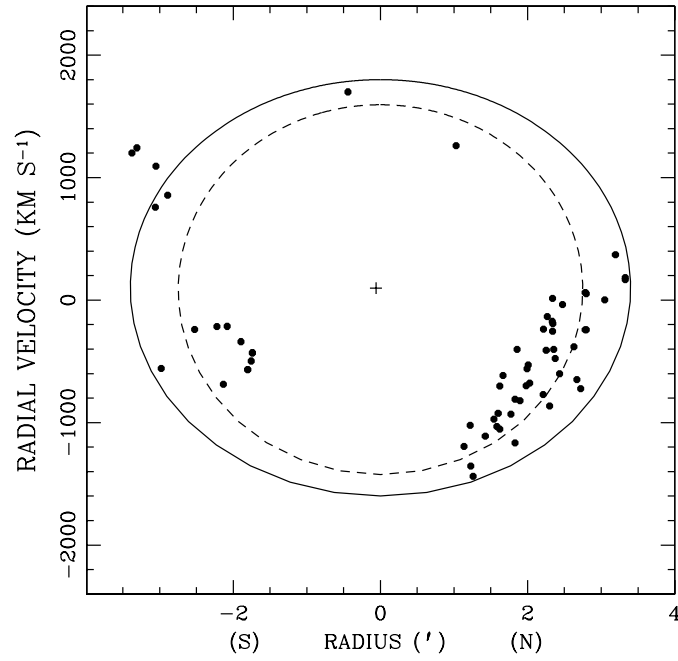


FIG. 6.— Radial velocity vs. projected radius for fast-moving knots in G292.0+1.8. Radii were measured from the geometric center of the radio image of the remnant (GW03). The solid line marks the best fit velocity ellipsoid that encompasses the outermost points of the velocity distribution, excluding the most redshifted southern FMKs. The dashed line marks the best fit averaged through all points of the velocity distribution.

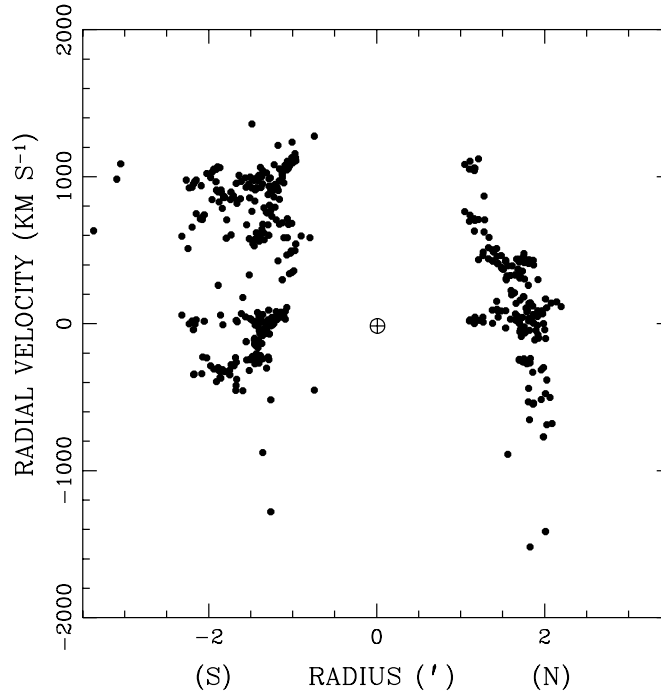


FIG. 7.— Radial velocity vs. projected radius for 462 points in the spur region of G292.0+1.8. The radii were determined as in Figure 6.

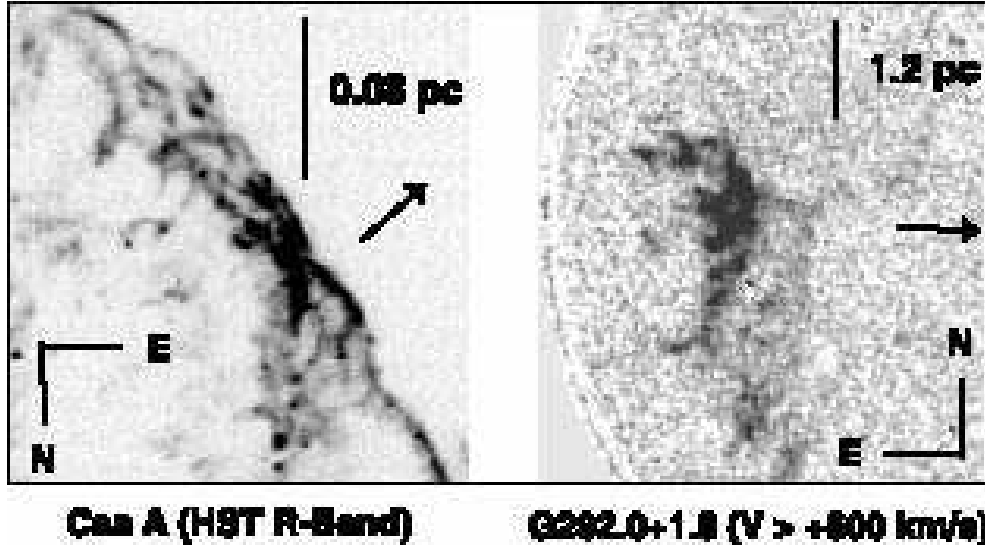


FIG. 8.— HST image of shocked ejecta in the northwest portion of Cas A (left panel, from Fesen et al. 2001) displayed beside an image of G292.0+1.8 (right panel) showing the summed [O III] emission from all redshifted RFP scans ($V \geq +600 \text{ km s}^{-1}$). For ease in comparing morphologies of the ejecta shells, the Cas A image has been rotated so that the expansion centers of the two SNRs (marked by the arrows) lie in roughly the same direction. Scale bars are shown for assumed distances of 3.4 kpc (Reed et al. 1995) for Cas A and 6 kpc (GW03) for G292.0+1.8. Despite the order of magnitude difference in spatial scale, both SNRs exhibit scalloped, concave filaments pointing away from the explosion center as would be expected for Rayleigh-Taylor unstable material recently compressed by the reverse shock. A full resolution figure can be found at <http://fuse.pha.jhu.edu/~parviz/papers/g292>.

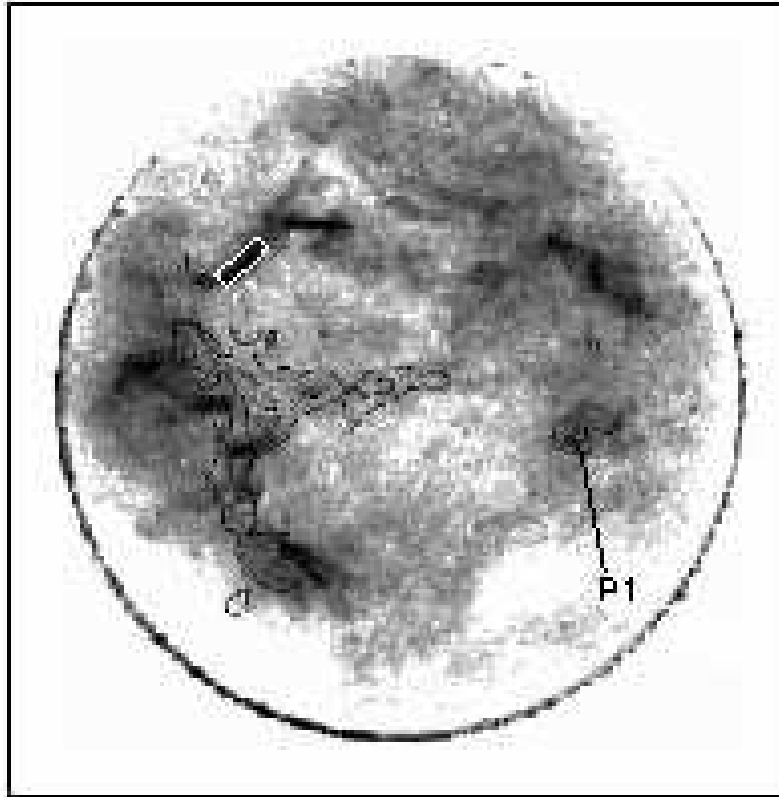


FIG. 9.— The zero-velocity $H\alpha$ image shown with logarithmic contours from the zero velocity [O III] image in Figure 2. There is little direct correspondence between [O III] and $H\alpha$ emission from the eastern spur, confirming that this feature is ejecta material. The extraction box for the spectrum in Figure 10 is marked on the filament with the white box. A full resolution figure can be found at <http://fuse.pha.jhu.edu/~parviz/papers/g292>.

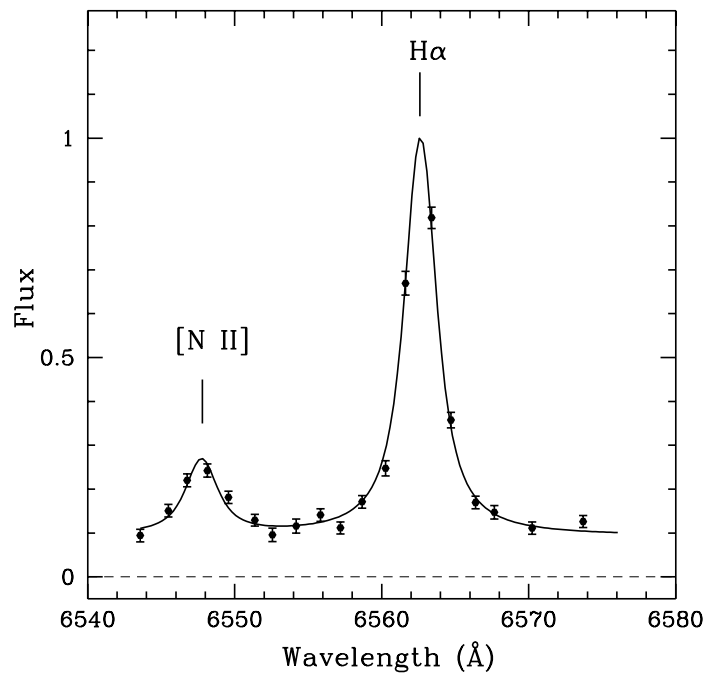


FIG. 10.— Sky-subtracted spectrum of a filament in the zero velocity $H\alpha$ image. Residual continuum is due to the presence of stars along the filament. The solid curve shows the best fits to the $H\alpha$ and $[N II] \lambda 6548$ line profiles.

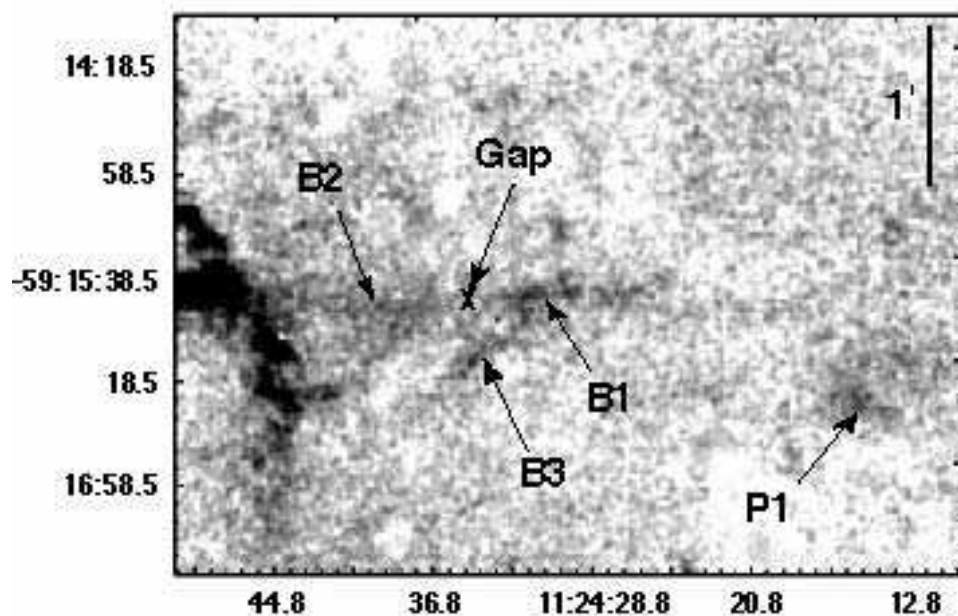


FIG. 11.— Closeup of the equatorial bar region in G292.0+1.8 in zero radial velocity $[O III]$ from the RFP scans (bottom). The features discussed in the text are marked. The 'X' marks the position of the geometric radio center measured by GW03. A full resolution figure can be found at <http://fuse.pha.jhu.edu/~parviz/papers/g292>.

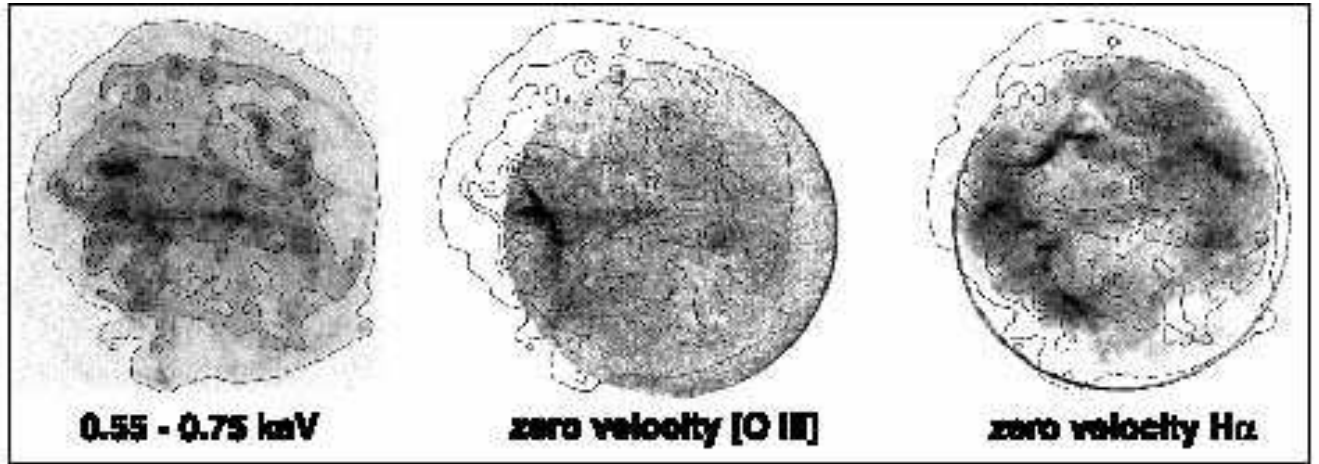


FIG. 12.— The *Chandra* X-ray image of G292.0+1.8 (shown far left) compared to the [O III] (middle panel) and H α (right panel) emission detected by the RFP at zero heliocentric radial velocity. Images are shown to the same spatial scale. The X-ray *Chandra* image has been filtered to show the oxygen line emission (0.55–0.75 keV) and has been adaptively smoothed to bring out the fine structure. Contours of the X-ray line emission are shown at logarithmic intervals of (0.05, 0.6, 1.07, 1.7, 2.6, 3.7 and 5.27) $\times 10^{-4}$ cts s $^{-1}$ arcsec $^{-2}$. These contours are overlaid onto all three images. A full resolution figure can be found at <http://fuse.pha.jhu.edu/~parviz/papers/g292>.

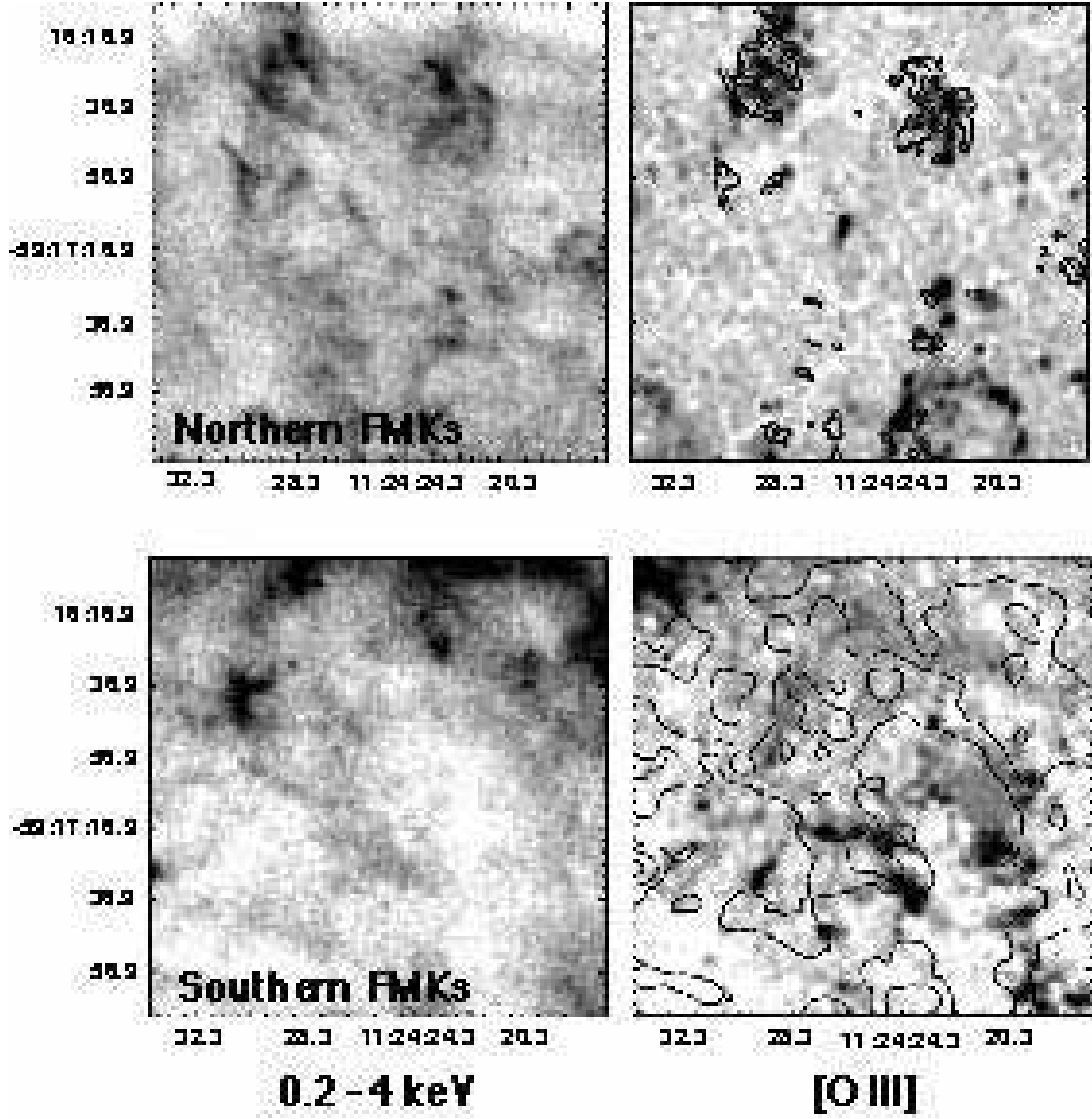


FIG. 13.— Closeup view of the northernmost and southernmost FMKs in G292.0+1.8, shown in the X-ray band (from *Chandra*, left panels) and in the narrowband [O III] image of WL05 (right panels). The images are displayed at the same spatial scale. (The large circular gray patch seen near the southern [O III] knots are the result of interpolation over a bright star.) Contours of X-ray emission are overlaid onto the optical image for comparison. The contours of the northern FMKs are spaced with a square root stretch at levels of $(5.9, 9.5, 8.2 \text{ and } 11.0) \times 10^{-4} \text{ cts s}^{-1} \text{ arcsec}^{-2}$. Contours of the southern FMKs are also spaced with a square root stretch at levels of 3.0×10^{-4} and $4.3 \times 10^{-4} \text{ cts s}^{-1} \text{ arcsec}^{-2}$. A full resolution figure can be found at <http://fuse.pha.jhu.edu/~parviz/papers/g292>.

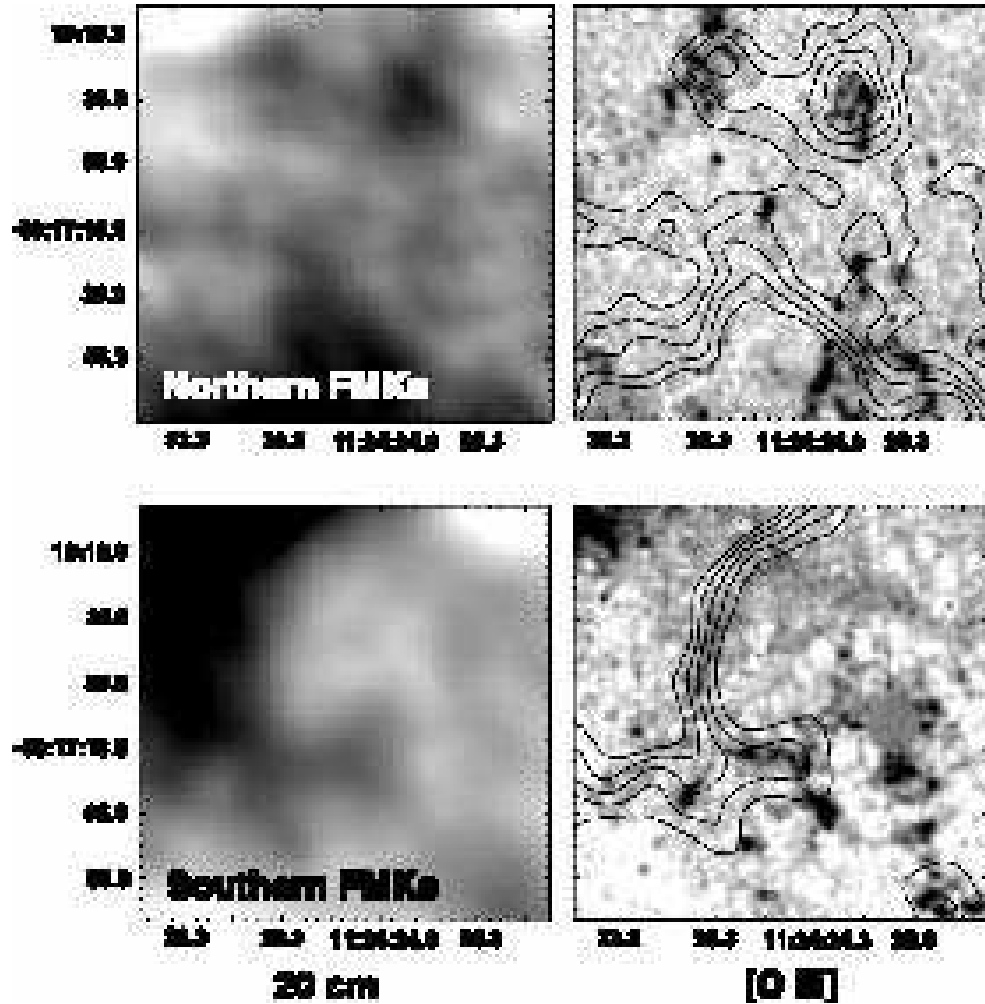


FIG. 14.— Closeup view of the northernmost and southernmost FMKs in G292.0+1.8, shown in the 20 cm radio continuum (GW03) (left panels) and in the narrowband [O III] image of WL05 (right panels). The images are displayed at the same spatial scale and correspond approximately to the same sky regions as fig. 13. Contours of the radio continuum are overlaid onto the optical image for comparison. The contours of the northern FMKs are spaced with a logarithmic stretch at levels of 3.5, 3.9, 4.0, 4.6 and 5.0 mJy beam⁻¹. Contours of the southern FMKs are also spaced logarithmically at levels of 6.5, 7.4, 8.0, 9.0 and 10.0 mJy beam⁻¹. A full resolution figure can be found at <http://fuse.pha.jhu.edu/~parviz/papers/g292>.